Diagnosing indirect-drive inertial-confinement-fusion implosions with charged particles

2010 Plasma Phys. Control. Fusion 52 124027

(http://iopscience.iop.org/0741-3335/52/12/124027)

Plasma Phys. Control. Fusion **52** (2010) 124027 (14pp) doi:10.1088/0741-3335/52/12/124027

Diagnosing indirect-drive inertial-confinement-fusion implosions with charged particles

C K Li[1], F H Séguin[1], J A Frenje[1], M Rosenberg[1], A B Zylstra[1], R D Petrasso[1], P A Amendt[2], J A Koch[2], O L Landen[2], H S Park[2], H F Robey[2], R P J Town[2], A Casner[3], F Philippe[3], R Betti[4,5], J P Knauer[4], D D Meyerhofer[4,5], C A Back[6], J D Kilkenny[6] and A Nikroo[6]

[1] Plasma Science and Fusion Center, Massachusetts Institute of Technology, Cambridge, MA 02139, USA
[2] Lawrence Livermore National Laboratory, Livermore, CA 94550, USA
[3] CEA, DAM, DIF, F-91297 Arpajon, France
[4] Laboratory for Laser Energetics, University of Rochester, Rochester, NY 14623, USA
[5] Department of Mechanic Engineering, and Physics and Astronomy, University of Rochester, Rochester, NY 14623, USA
[6] General Atomics, San Diego, CA 92186, USA

Received 16 June 2010, in final form 30 July 2010
Published 15 November 2010
Online at stacks.iop.org/PPCF/52/124027

Abstract

High-energy charged particles are being used to diagnose x-ray-driven implosions in inertial-confinement fusion. Recent measurements with vacuum hohlraums have resulted in quantitative characterization of important aspects of x-ray drive and capsule implosions. Comprehensive data obtained from spectrally resolved, fusion-product self-emission and time-gated proton radiographs with unprecedented clarity reveal new and important phenomena. Several types of spontaneous electric fields differing by two orders of magnitude in strength are observed, the largest being on the order of one-tenth of the Bohr field ($=ea_0^{-2} \sim 5 \times 10^{11}\,\mathrm{V\,m^{-1}}$, where a_0 is the Bohr radius). The hohlraum experiments demonstrate the absence of stochastic filamentary patterns and striations around the imploded capsule, a feature common to direct-drive implosions. The views of spatial structure and temporal evolution of spontaneous electromagnetic fields, plasma flows, implosion symmetry and dynamics provide insight into the physics of x-ray driven implosions. Potential applications for the National Ignition Facility are outlined.

(Some figures in this article are in colour only in the electronic version)

1. Introduction

Achieving inertial-confinement-fusion (ICF) ignition and high-energy gain is a primary goal of research on the National Ignition Facility (NIF) [1–4]. This scientific breakthrough is

being explored first with the indirect-drive approach [5–9] in which nearly Planckian x-ray radiation fields (hundreds of electronvolts) are generated by a 192-beam, 1.8 MJ high-power laser pulse irradiating a high-Z enclosure called a hohlraum. The x-ray radiation drives the implosion of a cryogenic deuterium–tritium (DT) capsule contained within a low-Z ablator. High temperature, high density and tremendous plasma pressure are achieved in the compressed core, potentially resulting in hot-spot ignition and a self-sustaining fusion burn wave that subsequently propagates into the main fuel region for high-energy gain.

Hohlraum-generated x-ray drive can create extreme plasma conditions and has served as an important platform for studying a wide range of basic and applied high-energy-density physics (HEDP) [10, 11], including laboratory astrophysics, space physics, nuclear physics and material sciences.

In diagnosing plasma conditions and field structures generated in a laser-irradiated hohlraum and in an imploded capsule, charged particles from either self-emission or backlighting [12, 13] can play an important role. Their interactions with plasmas are governed by the Coulomb force, while those with fields are governed by the Lorentz force. The plasma areal density (ρR)—a critical parameter of ICF implosions, is determined from the measured particle energy loss [14] through the relationship

$$\rho R = \int_{\varepsilon_0}^{\varepsilon} \rho \left(\frac{\mathrm{d}\varepsilon}{\mathrm{d}x} \right)^{-1} \mathrm{d}\varepsilon, \tag{1}$$

where ε (ε_0) is the particle (initial) energy. To precisely measure field strengths as well as unequivocally discriminate between electric ($\boldsymbol{E}$) and magnetic ($\boldsymbol{B}$) fields in the plasma, the Lorentz force

$$\boldsymbol{F} = q \left(\boldsymbol{E} + \frac{\boldsymbol{v} \times \boldsymbol{B}}{c} \right) \tag{2}$$

is used to quantify the relationship between field type and strength and deflections of a particle trajectory (where q is the charge and v is the velocity of a charged particle).

Despite their inherent sensitivity to plasma density and field structures, charged particles have not previously been used for diagnosing indirect-drive ICF implosions due to the complexity of the interactions. To date, diagnostics have relied on x- and gamma rays, visible or ultraviolet light and fusion neutrons. During the last two decades, advanced charged-particle diagnostics [15, 16] have been developed and implemented on the OMEGA laser facility [17] and have been used for studying direct-drive ICF implosions [18–26] and HEDP [27, 28]. These techniques are being explored for diagnosing indirect-drive ICF implosions on OMEGA and will be extended to the NIF.

In this paper, the fundamental concepts of diagnostics with charged particles are described, and the first measurements of indirect-drive ICF implosions with self-emitted charged-particle spectroscopy and monoenergetic proton radiography are presented. These methods make possible the observation and/or measurement of several important processes and parameters, including plasma flow, distributions of self-generated, dynamic E and B fields; ρR and implosion symmetry. In section 2, the method of diagnosing with self-emitted charged-fusion products is reviewed and the experimental results are presented. In section 3, the method of diagnosing with backlighting charged particles is outlined and the experimental results are presented. Implications for the NIF and future work are described in section 4 and the summary is presented in section 5.

2. Diagnostics with self-emitted charged-fusion products

The self-emitted charged particles of most interest for diagnosing ICF experiments are the implosion fusion products from several reactions such as the primary D^3He protons and DD protons resulting, respectively, from

$$D + {}^3He \rightarrow \alpha + p\ (14.7\,MeV) \tag{3}$$

and

$$D + D \rightarrow T + p\ (3.0\,MeV). \tag{4}$$

Protons result from the secondary D^3He reaction

$$D + {}^3He(0.82\,MeV) \rightarrow \alpha + p\ (12.6\text{–}17.5\,MeV). \tag{5}$$

Charged particles elastically scattered by primary neutrons (knock-on ions) from the fuel or shell [29] will be discussed in section 4. Other charged particles, either from primary, secondary [30] or tertiary fusion reactions [31] or from laser–plasma interactions [32], and their potential use in diagnosing indirect-drive ICF implosions are beyond the scope of this section and described elsewhere, for example [20]. In diagnosing fusion plasmas, the number and energy spectra of the charged-fusion products are directly related to the properties of the compressed core and imploded shell. Measurements of the charged-particle properties provide important information about fusion yields, fuel and shell temperatures, areal densities, implosion symmetry and dynamics, and fields in specific experiments, as well as information of general interest on such topics as the slowing down of energetic ions in ICF relevant plasmas [14].

Figure 1 schematically shows a typical vacuum, gold (Au) hohlraum and a warm plastic capsule filled with D^3He gas that were used in the indirect-drive experiments on OMEGA [33, 34] described in this paper. This OMEGA 'scale-1' hohlraum had a 1.6 mm diameter, a 2.45 mm length, 50% laser-entrance holes (LEH) and a 30 μm thick Au wall. The hohlraum was driven by 40 laser beams with a wavelength of 0.351 μm and a total laser energy ~19.7 kJ in a 1 ns square pulse. The laser beams had no spatial or temporal smoothing. The capsule was a ~50 μm thick plastic shell of diameter 660 μm filled with 50 atm D^3He gas. The typical radiation temperature was ~240 eV, and produced a proton yield of $\sim 10^{10}$.

Several charged-particle diagnostics, including wedge-range-filter (WRF) spectrometers [15], spectrally resolved proton imaging [13] and a CR-39 based proton fluence imaging system [15], were arranged along or perpendicular to the hohlraum axis (i.e. polar or equatorial). The utility of these charged-fusion products in a specific implosion depends on their penetration and range in plasmas. To explicitly illustrate this, figure 2 shows the calculated proton residual energy as a function of its penetration in an imploded CH shell and then in a gold hohlraum wall.

Figure 3 shows self-emitted, spectrally resolved one-dimensional images and associated energy spectra, as well as fluence images collected from D^3He protons produced during the nuclear burn in an implosion [13, 33, 34]. A number of critical implosion quantities were obtained from these measurements, including fusion yields, ρR, and ρR asymmetries. Fusion protons were generated at two different times (~200 ps separation for the implosions presented herein): when the shock wave converges at the center of the imploded core (shock flash) and later when fuel burn occurs near the capsule peak compression (compression burn). The proton yields associated with shock-coalescence burn (the narrow high-energy peak) and with compressive burn (the broad low-energy peak) are clearly measured by the energy spectra and spectrally selected images. Values of ρR inferred from measured proton energy losses indicate that ~23 mg cm^{-2} is achieved at shock-flash time and ~77 mg cm^{-2} at the compressive burn

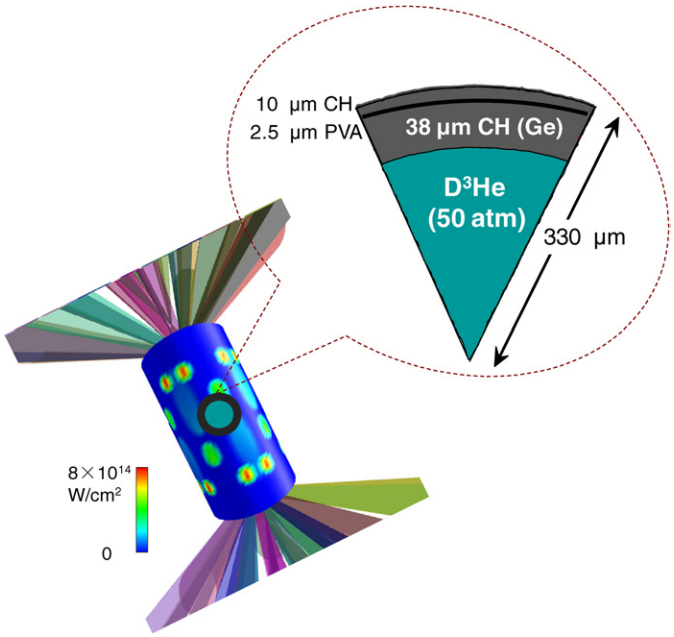

Figure 1. Schematic diagrams of a cylindrical hohlraum used in the experiments with a plastic capsule filled with D^3He gas. Entering each end of the hohlraum were 20 laser beams: 5 with incidence angle 21.4° (cone 1 in OMEGA laser configuration), 5 with incidence angle 42° (cone 2) and 10 with 58.8° (Cone 3). The lighter area shown on the hohlraum wall indicates the locations of the laser spots (modeled by VISRAD [35]). Charged-particle diagnostics were arranged along the poles and equator [33, 34].

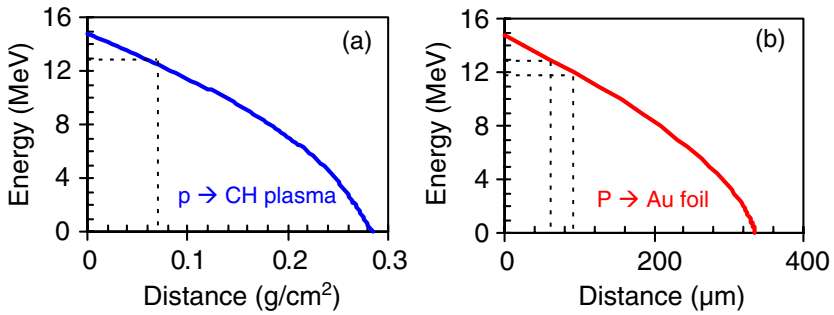

Figure 2. The residual energy of a D^3He proton is plotted versus its distance traveled (ρR) in CH plasma (a) and in a Au foil (b). It is seen that a 14.7 MeV proton loses ∼2 MeV after penetrating $\rho R \sim 70\,\mathrm{mg\,cm^{-2}}$ of a CH plasma (CH shell of an imploded capsule with $\rho = 20\,\mathrm{g\,cm^{-3}}$, $T_e = 500\,\mathrm{eV}$), then loses another ∼1 MeV after penetrating a 30 μm thick Au hohlraum wall.

time for both the polar (along the LEH) and equatorial directions (after correcting for the extra energy loss due to proton passing through the 30 μm hohlraum wall). This suggests that the implosion is quite symmetric (the level of asymmetry is within the diagnostic uncertainty), as expected from experimental design. The spatial structure of the proton flux along the LEH appears to be nonuniform (compared with the image along the equator) at shock flash and compression burn phase, indicating deflection of the proton flux.

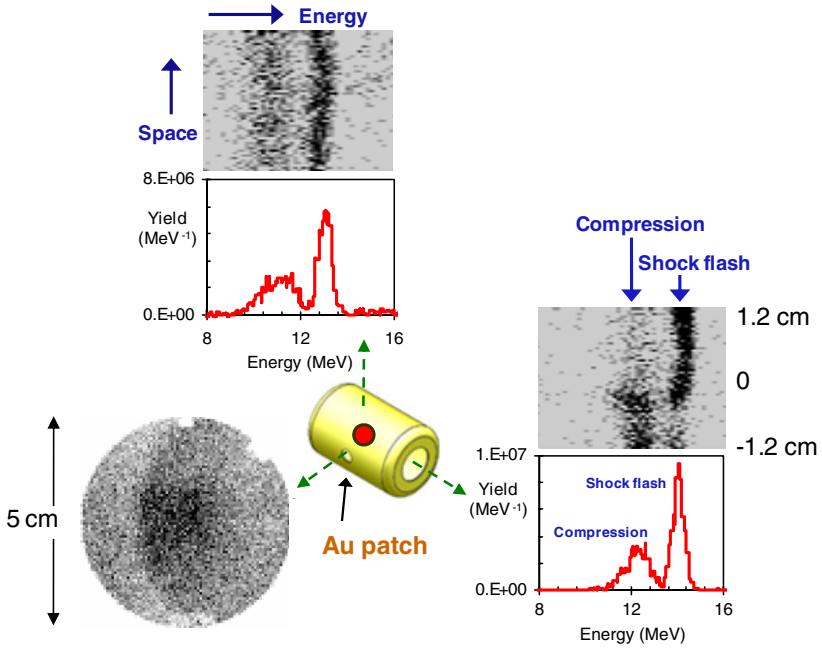

Figure 3. Spectra and images of self-emitted protons generated from the fusion reaction of D and ^{3}He in an indirectly driven ICF implosion (OMEGA shot 54744), measured simultaneously along three different directions. The narrow high-energy peak in each spectrum is associated with shock-flash burn and the broad low-energy peak with compression burn. The fluence image along the equator shows the edge of a patch on the hohlraum wall, and demonstrates that the fluence was fairly uniform. (Reprinted from [13].)

To further address these nonuniformities, implosions with rugby-shaped hohlraums and equivalent experimental conditions, including the targets and laser drive, were performed [33, 34]. Figure 4 shows self-emission, spectrally resolved one-dimensional images and an energy spectrum, as well as fluence images collected from different directions. While the proton fluence in the direction of the equator is spatially uniform, the fluence in the direction of the LEH shows nonuniformity with a spatial variation ∼1–2 cm at the detector plane (figure 4). This scale is similar to that observed along the LEH in the cylindrical hohlraum implosion (figure 3), where a scale ∼1.2 cm nonuniformity at two different energy components was measured with the spectral resolved image.

For cylindrical hohlraum experiments (figure 3) these protons were generated at different times (separated by about ∼200 ps between the shock flash and compression burn), and the fluence nonuniformities have significantly evolved over this time interval. They are not likely to have been caused by proton collisional scattering from the plasma, because the measured proton energies along LEH and the equator are very similar. This suggests that the proton fluence nonuniformities are due to self-generated B or E fields near the LEH that do not change the proton energy but deflect their trajectories. If they are due to a B field, its strength is estimated to be $\sim 2.5 \times 10^5$ T μm. Taking an approximate scale length of 500 μm (∼20% of the hohlraum length, a rough estimate since the plasma density scale length is shorter than a quarter of the hohlraum length), the B field would be about 500 T (5 MG). If the nonuniformities are due to an E field, the strength required is $\sim 5 \times 10^{10}$ V m^{-1}, about one-tenth of the Bohr field—a fundamental field strength for stripping bound electrons—which effectively enhances

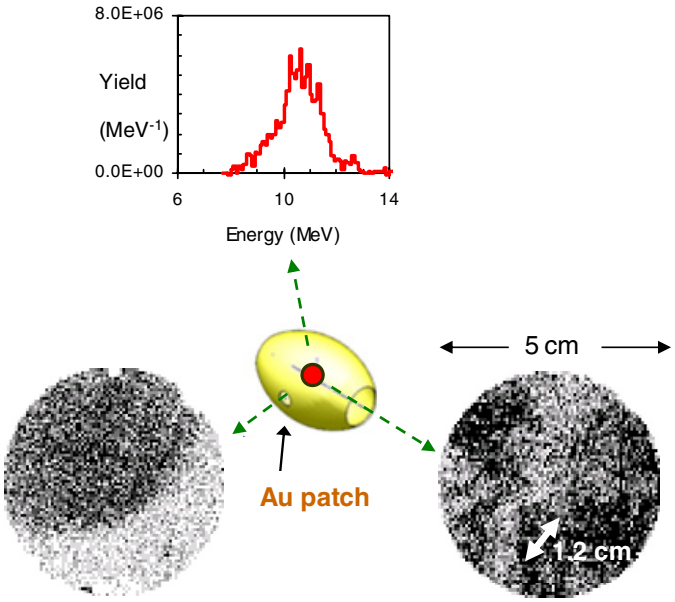

Figure 4. The spectra and images of self-emitted protons generated from the fusion reaction of D and ^{3}He in OMEGA shot 54741, measured simultaneously in three different directions relative to a rugby-shaped hohlraum. Compared with the self-emission image made in the equatorial direction, the one recorded through the LEH shows very nonuniform proton fluence [33, 34]. The shock-flash yield is minimal in this implosion, probably as a consequence of nonuniform implosion due to the capsule being slightly off of the hohlraum center (which leads to poor shock coalescence both spatially and temporally, resulting in a lower ion temperature).

and sustains the ionization after the laser is turned off (∼1.1 ns). Note that for this implosion the shock-flash time is ∼1.7 ns and the compression burn time is ∼1.9 ns. The high fields are likely generated in the region near the LEH where the outward-directed axial plasma becomes increasingly resistive after the laser drive ends, leading to the generation, growth and saturation of magneto-instabilities, driven by the plasma pressure gradient ($\gamma \propto \nabla P_e$, where γ is the growth rate) [36, 37]. The data suggest that the spatial structure or the directions of such fields undergoes rapid changes between the time of shock flash and compression burn [13].

3. Backlighting with charged particles

A novel platform that combines a monoenergetic-particle backlighter with a matched detection system [15, 27] , shown in figure 5, has been implemented on OMEGA and can be implemented at the NIF. The backlighting protons are fusion products (14.7 MeV D^{3}He protons and 3 MeV DD protons) that are generated from an exploding-pusher implosion of a thin-glass capsule filled with D^{3}He gas. The proton yields ($>10^8$ over 4π steradians) are usually adequate for backlighting a typical subject. Such yields should be readily achieved on the NIF using a small number of laser beams since an exploding-pusher implosion is insensitive to drive asymmetry [27].

To break the degeneracy among the different possible mechanisms of bending backlighting proton trajectories, we consider whether the image features seen in the region between the capsule and the hohlraum wall are due to collisional scattering in the plasma or to proton deflections by E or B fields. This analysis is helped by the fact that nearly simultaneous

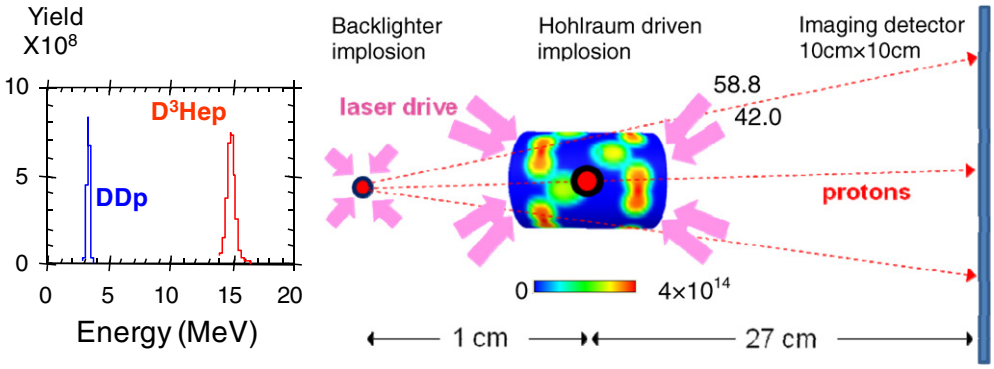

Figure 5. Experimental setup. Shown are the proton backlighter (imploded D^3He-filled thin-glass-shell capsule, driven by 30 OMEGA laser beams), a Au hohlraum, a CR-39 imaging detector and 30 laser beams. On each end of the hohlraum, 5 beams had incidence angle 42° (cone 2 in OMEGA laser configuration) and 10 beams had incidence angle 58.8° (cone 3). The end-on backlighting protons pass through the laser-driven hohlraum, sampling hohlraum conditions and capsule implosions. The imaging detector is a 10 cm × 10 cm CR39 track detector. The lighter area shown on the hohlraum wall indicates the locations of the laser spots (modeled by VISRAD). Proton radiography images of hohlraum-driven implosions at different times are shown in [13] and figure 7.

images are recorded with two different but very accurately known initial proton energies. It follows from the Lorentz force law that deflection angles due to B are inversely proportional to the square root of the proton energy ε_p [38],

$$\theta(\boldsymbol{B}, \varepsilon_p) \propto \frac{1}{\sqrt{2m_p\varepsilon_p}} \left| \int \boldsymbol{B} \times \mathrm{d}\ell \right|; \tag{6}$$

while those due to E are inversely proportional to the proton energy [38],

$$\theta(\boldsymbol{E}, \varepsilon_p) \propto \frac{1}{2\varepsilon_p} \left| \int \boldsymbol{E} \times \mathrm{d}\ell \right|. \tag{7}$$

The energy scaling due to collisional scattering (the characteristic scattering angle in radians) is also inversely proportional to the proton energy [38]

$$\theta(\varepsilon_p) \propto \frac{1}{2\varepsilon_p} \sqrt{\frac{\rho L}{\rho L_{\mathrm{rad}}}}, \tag{8}$$

where ρL is the plasma areal density; ρL_{rad} is the radiation length (equivalent areal density of a specific material, for example, $\rho L_{\mathrm{rad}} \approx 4.3 \times 10^4$ mg cm^{-2} for carbon and $\approx 6.5 \times 10^3$ mg cm^{-2} for gold [39]). Figure 6 plots the deflection as a function of energy for these different energy scalings. The energy scaling due to B is unique, while those due to E and collisional scattering are degenerate. Since deflections due to collisional scattering are accompanied by an energy loss, while those due to transverse E fields are not, discrimination between the two effects is possible.

Figure 7 shows end-on radiographs of 15 MeV D^3He protons and 3 MeV DD protons covering a typical indirect-drive ICF implosion sequence (the experimental setup is shown in figure 5). The hohlraums were the OMEGA scale-1.5 size with 30 μm thick Au walls overcoated with 0.3 μm CH, 100% LEH, 2.4 mm diameter and 3.8 mm length. Each hohlraum was driven by 30 laser beams forming four irradiation rings with total laser energy ~11 kJ in a 1 ns square pulse. In these backlighting experiments the individual laser beams had full

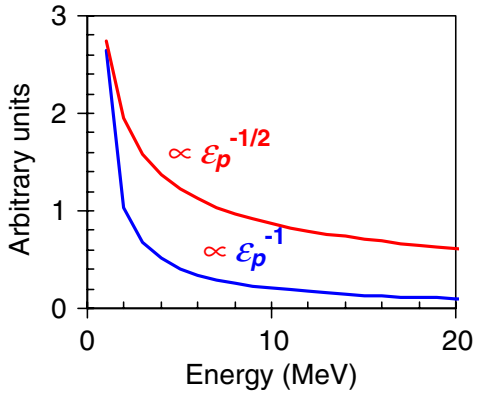

Figure 6. Calculated proton deflection angles plotted as a function of proton energy. The deflection scales differently with proton energy ε_p for B field ($\propto \varepsilon_p^{-1/2}$) and E field ($\propto \varepsilon_p^{-1}$). Collisional scattering scales with energy the same as E-field deflection does, but the degeneracy between them sometimes can be broken when proton energy loss is taken into account.

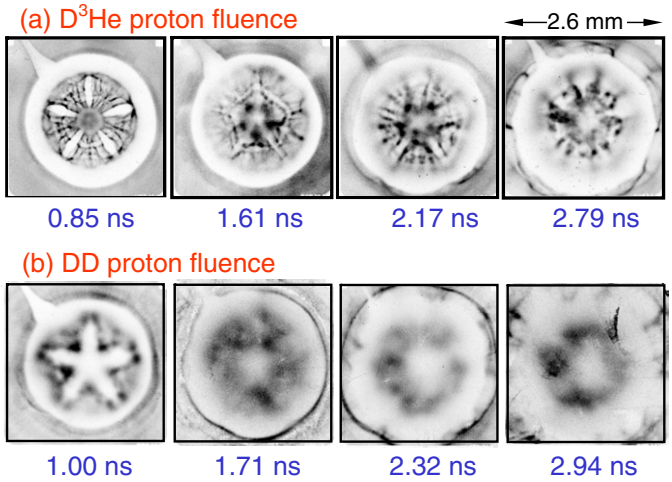

Figure 7. Radiographs of laser-driven hohlraums with CH-shell capsules made with 15 MeV protons (*a*) and 3.3 MeV protons (*b*). Within each image, darker means higher proton fluence, and the capsule-mounting stalk appears in the upper left corner. The slightly different times in (*b*) are due to the slower proton velocities and longer flight times, and the smeared spatial structures are caused by fields and scattering. These images illustrate temporal evolution of the fields, plasma flow and implosions. (Reprinted from [13].)

spatial and temporal smoothing [18]. The images are displayed to show proton fluence versus position, providing time-dependent information about field distributions, capsule compression and hohlraum plasma conditions (though each time comes from a different shot). A striking feature in these images is a five-pronged, asterisk-like pattern surrounding the imploding capsule, a consequence of the laser-beam positions on the hohlraum wall. A simulation of the laser intensity distribution associated with the OMEGA 58.8°- and 42.0°-beam configurations is shown in figure 8, viewed from a location just outside the LEH. The ten 58.8° laser beams are grouped to form five pairs with 26.8° between two beams within each pair, but 45.2° between

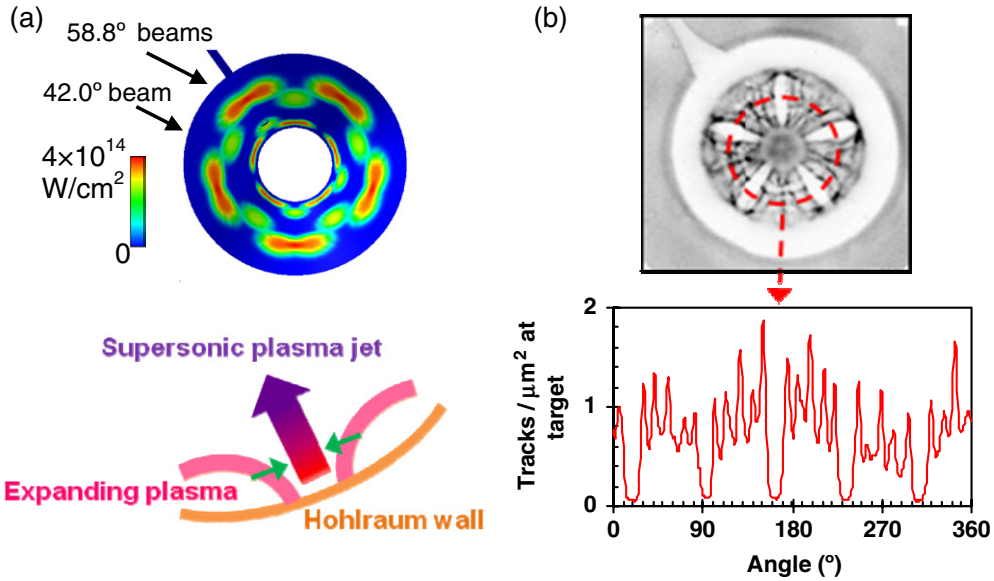

Figure 8. (*a*) The laser intensity distribution associated with the OMEGA 58.8°-beam and 42°-beam configurations, as viewed from just outside of the LEH (modeled by VISRAD) and a cartoon illustrating the formation of a supersonic, radially directed plasma jet (spoke) as two laser-driven expanding plasma bubbles approach one another. (*b*) An azimuthal lineout of the 0.85 ns image of figure 7 indicates that the periodic pattern is associated with the 'near' and 'far' laser-beam distributions (relative to the detector). (Reprinted from [13].)

adjacent pairs (figure 8). An azimuthal lineout of the fluence image (figure 8(*b*)) indicates that the asterisk spokes are formed between two expanding plasma bubbles that are generated by 'nearest neighbor' (58.8°) laser-beam pairs (figure 8(*a*)), while the periodic patterns (narrow fingers) between these spokes are associated with the remaining laser-beam distributions from both hohlraum ends. Similar plasma jets and asterisk-like image patterns have been observed from x-ray self-emission on Nova 10-beam laser–hohlraum interactions [40]. The higher x-ray emission from the hohlraum center and the regions between the two approaching plasma bubbles indicate that the hohlraum stagnation resulted in higher plasma temperature and density.

For a physical picture of the formation of the asterisk spokes, we consider the expanding plasma bubbles (electron temperature $T_e \sim 1$ keV, ion temperature $T_i \sim 10$ eV and electron density n_e (in units of critical electron density at 0.35 μm)$\sim 0.1 n_c$) generated on the hohlraum wall near the laser spots, governed by plasma hydrodynamics since the plasma thermal pressure is much larger than the magnetic pressure. Their hydrodynamic expansion is determined by the sound speed ($C_s \sim (ZT_e m_i^{-1})^{1/2} \sim 250\,\mu$m ns^{-1} for CH and $\sim 150\,\mu$m ns^{-1} for Au, where Z is the average ion charge state). For an adiabatic rarefaction expansion of an ideal gas, the expansion speed is $3C_s$, close to the observed jet speed ($\sim 4C_s$) [12, 13]. The hot electrons advancing ahead of the rarefaction expansion due to their high mobility may further boost the motion of leading edge CH and Au ions ablating off the hohlraum wall by an additional sound speed ($\sim C_s$) factor. Since the separation between the electrons and ions is on the order of a Debye length (λ_D) and an ion inertial response is on the order of an ion plasma frequency (ω_{pi}), a representative speed is obtained: $C_s = \lambda_D \omega_{pi}$. With $\sim 200\,\mu$m between pairs of bubbles [12], it is observed that adjacent CH bubbles coalesce in ~ 0.1 ns and reach the hohlraum axis in ~ 1 ns, with the Au plasma bubble trailing behind [13].

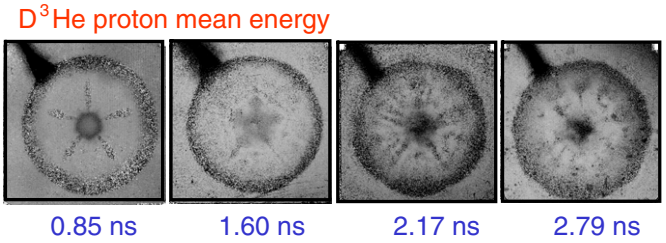

Figure 9. Images showing mean proton energy as a function of position for the fluence images of figure 7(*a*) (within each image, darker means more proton energy loss and therefore more matter traversed). The gray-scale mapping for image display is different in each image. The capsule-mounting stalk appears in the upper left corner of each image. (Reprinted from [13].)

The B field can be excluded by symmetry. The five-pronged asterisk-like pattern shown in figures 7 and 8 provides a constraint that rules out the possibility of self-generated B fields as a major cause for the formation of this structure, since the toroidal B-field topology around the laser spots or radial jets cannot result in azimuthal proton deflections. With the B field excluded, the other two possible mechanisms for deflecting the proton trajectories are intense, local E fields associated with strong azimuthally oriented electron pressure gradients (∇p_e) in the spokes and proton scattering in the spokes.

The possibility that the proton deflection is mostly caused by scattering that deflects protons out of the dense spoke can be ruled out through the measurements of the proton energy loss. It can be shown (figure 9, $t = 0.85$ ns) that there is little energy loss for protons passing through the major spokes. In the regions between the five spokes (figure 7 and 8), there are high-contrast features in the fluence image, including the counterparts of the spokes generated by the 'far' beams on the other side of the hohlraum, but very little variation in energy (figure 9).

This leaves the E fields as the remaining cause. Using the spoke widths estimated in the images, $\int \boldsymbol{E} \times \mathrm{d}\ell \sim 3 \times 10^5$ V (where $\mathrm{d}\ell$ is the differential path length along the proton trajectory through the field area). Taking a scale length $\sim$1 mm (the size of a laser spot) for the field in a jet-spoke results in $E \sim 3 \times 10^8$ V m^{-1} with field directions pointed away from the spoke. This is the first time such strong, local E fields inside the hohlraum have been inferred even though the cavity is effectively a Faraday cage [13]. The effects of such fields may impact important physics issues, including laser–plasma instabilities, modification of the plasma electron distribution and implosion symmetry.

Whereas the structures of asterisk-like spokes and narrow fingers inside the hohlraums (figure 8(*b*)), were largely the result of the 15 MeV proton deflection by internal E fields (figure 7(*a*)), the apparent increasing hohlraum size with time, as shown in figure 7(*b*), is attributed to the 3 MeV protons scattered off the plasmas from the CH liner flowing out of the hohlraum ends, since the positive potential on the hohlraum wall [12] has largely decayed even before the end of the laser pulses, as indicated by the laser-irradiated unlined hohlraums [12].

4. Charged-particle diagnostics for indirect-drive ICF implosions at the NIF

This work will be extended using the unique capabilities of the NIF (i.e. substantially more laser beams and energy, enhanced pulse shaping capabilities and pulse durations, and greatly improved symmetry, etc). Compared with the OMEGA experiments, the proposed NIF ones include larger spatial- and temporal-scale plasmas inside the hohlraum and imploded capsule. To obtain the drive symmetry required for achieving ignition, the hohlraums will be filled

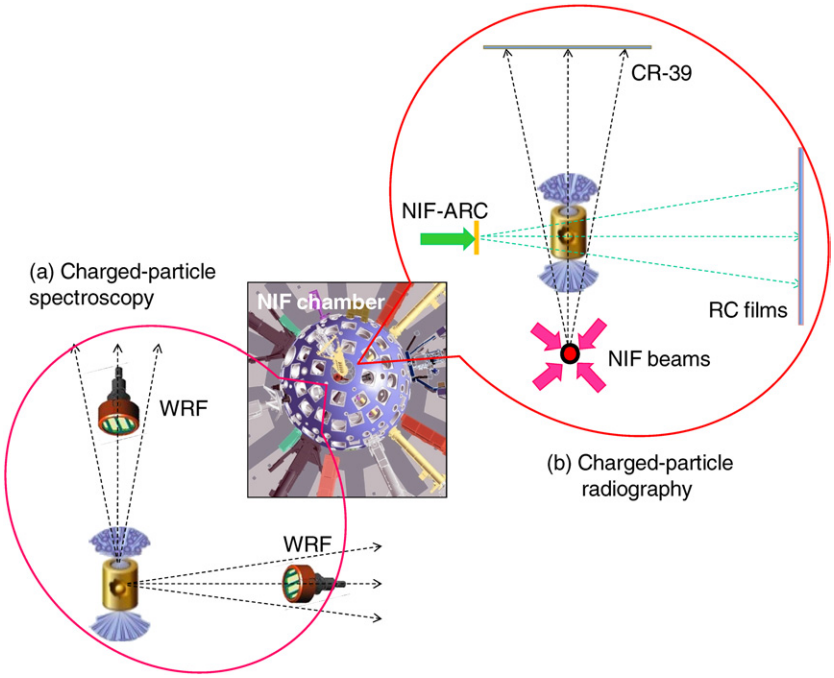

Figure 10. Schematic diagrams of proposed experiments in the NIF target chamber. (*a*) Proposed charged-particle spectroscopy measurement of self-emitted D^3He protons with WRF spectrometers used simultaneously in a number of directions, particularly along the poles and equator. (*b*) Proposed proton backlighting experiments for joint imaging of the electromagnetic fields inside/outside the hohlraum at the NIF. In these experiments, a total of eight NIF beams from opposite quads will be used to drive the backlighter implosions (exploding-pusher mode) which will radiograph the hohlraum from the direction of the pole. The remaining NIF beams will be arranged to drive a gas-filled hohlraum. Protons generated by a NIF-ARC petawatt beam will be used to radiograph the hohlraum from the equatorial direction.

with a low-Z gas ($\sim 0.04 n_c$) that is expected to minimize the motion of Au plasma in the laser-deposition region. A thin polyimide window covering each LEH will be used to initially contain the gas fill. Knowledge of plasma flow and fields inside gas-filled hohlraums is critical for understanding and modeling the performance of the ignition implosions at the NIF [5–9].

Figure 10 shows a schematic diagram for a NIF indirect-drive implosion experiment. In figure 10(*a*), several WRF spectrometers are placed in different directions (primarily along the poles and equator) and will be used to measure particles from different directions for implosion symmetry and dynamics studies. Because a finite number of spectrometers can be used simultaneously and each spectrometer samples a significant angular fraction of a capsule's surface, only low-mode-number perturbations are detected. Such diagnostics are important for determining the low-mode number implosion asymmetry, particularly the P2 Legendre mode, for the NIF campaign of Symmetry Capsule (SymCap) implosions.

Another important measurement on the NIF will be the remaining ablator mass of any failed ignition-capsule implosion that is critical for understanding and controlling implosion dynamics and for careful tuning of drive conditions. Inadequate knowledge about the drive physics is a serious concern, since an underdriven or overdriven capsule will result in too much or too little ablator mass as payload, leading to reduction of implosion performance and possibly a failure to ignite [2, 41, 42]. This is because if the initial ablator is too thin, it burns

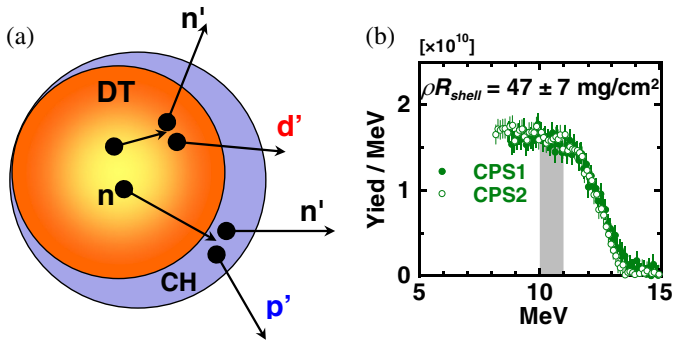

Figure 11. (*a*) A schematic of the knock-on processes in an asymmetrically imploded capsule to illustrate the probing of remaining ablator mass. Primary 14.1 MeV DT neutrons, generated in the fuel, elastically scatter deuterons out of the fuel and protons out of the shell. Information from the compressed core is carried out by these knock-on deuterons and information from the compressed shell is carried out by KO-ps. (*b*) A KO-p spectrum in the flat region between 10 and 12 MeV has been used to infer the areal density. The endpoint of this spectrum is about 14 MeV, reflecting the fact that particles scattered from the outer part of the shell have no energy loss. For this shot, measurements from CPS1 and CPS2 were similar, suggesting ablator mass remaining in these two directions was very similar [29].

through too quickly and the implosion fails to ignite due to preheat or instability issues; or if the initial ablator is too thick, the implosion velocity is too low and the implosion fails to ignite due to poor compression [2, 41, 42].

By fielding compact proton spectrometers at various locations around the implosion, the ρR and its asymmetries for a failed implosion can be obtained through absolute measurements of knock-on proton (KO-p) spectra

$$\mathrm{n}(14.1\,\mathrm{MeV}) + \mathrm{H} \rightarrow \mathrm{n}'(<14.1\,\mathrm{MeV}) + \mathrm{p}'(<14.1\,\mathrm{MeV}), \tag{9}$$

and knock-on deuterium (KO-D) spectra

$$\mathrm{n}(14.1\,\mathrm{MeV}) + \mathrm{D} \rightarrow \mathrm{n}'(1.6\text{–}14.1\,\mathrm{MeV}) + \mathrm{d}'(< 12.5\,\mathrm{MeV}). \tag{10}$$

Figure 11(*a*) shows a cartoon to illustrate the issue of remaining ablator mass in an asymmetrically ablated CH-shell implosion and directional KO-p spectrum (figure 11(*b*)) measured from an OMEGA shot (the KO-p yields and shapes from different directions are directly related to the remaining CH mass) [29]. We are extending this technology to the experiments of the NIF Ignition Campaign (NIC). For ignition capsules with a Cu-doped beryllium ablator, a 50–50 mixture of DT fuel and ∼1% residual hydrogen H by atom, failed implosions would result in neutron yields ranging from $\sim 10^{11}$ to $\sim 6 \times 10^{15}$ [29]. For capsules with an ablator of Ge-doped CH, which contains large amounts of H, failed implosions would result in neutron yields ranging from $\sim 10^{10}$ to $\sim 6 \times 10^{15}$ and local ρRs up to $\sim 200\,\mathrm{mg\,cm^{-2}}$. Prior to the ignition experiments, capsules with a Cu-doped Be ablator or Ge-doped CH ablator, more deuterium-lean fuel mixture and H-dopant levels up to 25% in the fuel [29] will be imploded to primarily reduce the neutron yield. The tritium–hydrogen–deuterium (THD)-filled Be-capsule implosion, which would result in neutron yields ranging from $\sim 5 \times 10^9$ to $\sim 6 \times 10^{15}$, can be adequately diagnosed with KO-ps since the signal-to-background ratio is significantly higher than that of an ignition-capsule implosion.

The proposed proton backlighting experiment for joint imaging of the electromagnetic fields inside/outside the hohlraum at the NIF is shown in figure 10(*b*). Radiographs made with 15 MeV protons and 3 MeV protons from ignition-like implosions will be used to measure the

generation, evolution, instabilities and effects of spontaneously generated E and B fields inside a hohlraum and inside an imploded capsule; and to study the effects of fill-gas on impeding plasma flows and on implosion performance. Proton yields ($>10^8$ over 4π steradians) are quite adequate for backlighting a typical subject. Importantly, these yields should be readily achieved using a small number of NIF laser beams from two opposing quads. Specifically, eight NIF beams (total 20–50 kJ energy in various pulse shapes) from two opposite quads (one top and one bottom from opposing 23° beams) will drive a thin-glass-shell capsule (∼2.1 mm diameter with ∼5 μm thick shell) filled with D^3He gas (∼20 atm, equal number of particles). The remaining NIF laser beams will be arranged to drive the subject targets with various pulse shapes and laser energies. These subjects will be ignition-relevant indirect-drive ICF targets (for example, a standard Au hohlraum (NIF scale 1-1.5) with a 50 μm thick CH shell filled with 50 atm H_2 gas, or standard 'SymCaps'). The backlighter will be placed about ∼2 cm from TCC toward (180°, 0°) and will be held by the warm-target positioner. The hohlraum will be placed at TCC by the cryogenic target positioner. The imaging detector will be placed ∼30–50 cm toward the polar direction. The timing of the backlighter relative to hohlraum drive can be adjusted to sample implosions at different times.

Simultaneous backlighting of ignition-relevant implosions will be done from nearly orthogonal directions with protons generated by NIF beam-drive exploding-pusher implosions and by NIF-ARC short-pulse laser–foil interactions (figure 10(*b*)) which backlight the hohlraum from the equatorial direction. ARC-generated protons have a much broader spectrum and nonisotropic (strongly forward peaked) emission in both fluence and energy, along with unique advantages such as higher spatial resolution (<10 μm) obtainable with a smaller effective source size, a shorter source duration for better time resolution (<10 ps) and a higher proton energy (∼50 MeV) for imaging ICF implosions and hohlraums with higher areal densities and less proton scattering [32]. The backlighter target will be a Au or Cu foil 2 mm × 2 mm in size and 10–50 μm thick (protons come from H impurity on targets preferentially accelerated due to highest Z/M by hot electrons). The much higher proton fluences and broad spectra from this foil backlighter may necessitate the use of a different imaging detector, possibly a stack of well-characterized radiochromic films [43]. Although there are trade-offs with the petawatt backlighters (as noted above), it may be possible to use the potentially higher proton energies to image high-areal-density, direct-drive ICF capsule implosions (such as those generated with low-adiabatic drive pulses) and to image laser-driven hohlraums from the side, looking through the walls.

5. Summary

Diagnosing of indirect-drive implosions in ICF with charged particles is explored experimentally at the OMEGA laser facility and extensions to the NIF are considered. Recent measurements with vacuum hohlraums have shown the feasibility of such diagnostics, and have resulted in characterizations of aspects of x-ray drive and capsule implosions. Comprehensive data obtained from advanced spectrally resolved, fusion-product self-emission and through time-gated proton radiograph imaging of unprecedented clarity have revealed a number of new phenomena. In particular, several types of spontaneous electric fields differing by two orders of magnitude in strength, the largest being on the order of one-tenth of the Bohr field ($\sim 5 \times 10^{11}$ V m^{-1}), were observed. The experiments demonstrate the absence of the stochastic filamentary patterns and striations appearing around the imploded capsule, a common feature occurring in direct-drive ICF implosions. The methods have allowed us to make observations of plasma flow and supersonic plasma jets (∼Mach 4); to probe distributions of self-generated, megagauss dynamic B fields; to determine ρR and implosion symmetry and to characterize

implosion dynamics. Potential applications of such advanced charged-particle diagnostics to experiments at the NIF have been described.

Acknowledgments

This work was supported in part by the US DOE and LLE National Laser User's Facility (DE-FG52-07NA28059 and DE-FG03-03SF22691), LLNL (B543881 and LDRD-ER-898988), CEA/DIF (France, Cooperative agreement No. DE-FC52-08NA28302), LLE (414090-G), FSC at Universty of Rochester (412761-G) and General Atomics (DE-AC52-06NA27279).

References

[1] Nuckolls J *et al* 1972 *Nature* **239** 139
[2] Lindl J D 1999 *Inertial Confinement Fusion* (New York: Springer)
[3] Atzeni A and Meyer-Ter-Vehn J 2004 *The Physics of Inertial Fusion* (Oxford: Clarendon)
[4] McCrory R L *et al* 2008 *Phys. Plasmas* **15** 055503
[5] Glenzer S H *et al* 2010 *Science* **327** 1228
[6] Landen O L *et al* 2010 *Phys. Plasmas* **17** 056301
[7] Froula D H *et al* 2010 *Phys. Plasmas* **17** 056302
[8] Meezan N B *et al* 2010 *Phys. Plasmas* **17** 056304
[9] Michel P *et al* 2010 *Phys. Plasmas* **17** 056305
[10] Davidson R C 2003 *Frontiers in High Energy Density Physics* (Washington, DC: National Academies Press)
[11] Drake R P 2006 *High-Energy-Density Physics* (New York: Springer)
[12] Li C K *et al* 2009 *Phys. Rev. Lett.* **102** 205001
[13] Li C K *et al* 2010 *Science* **327** 1231
[14] Li C K and Petrasso R D 1993 *Phys. Rev. Lett.* **70** 3059
[15] Séguin F H *et al* 2003 *Rev. Sci. Instrum.* **74** 975
[16] Frenje J A *et al* 2004 *Phys. Plasmas* **11** 2798
[17] Soures J M *et al* 1996 *Phys. Plasmas* **3** 2108
[18] Meyerhofer D D *et al* 2001 *Phys. Plasmas* **8** 2251
[19] Li C K *et al* 2002 *Phys. Rev. Lett.* **89** 165002
[20] Petrasso R D *et al* 2003 *Phys. Rev. Lett.* **90** 095002
[21] Zhou C D *et al* 2007 *Phys. Rev. Lett.* **98** 025004
[22] Rygg J R *et al* 2008 *Science* **319** 1223
[23] Li C K *et al* 2008 *Phys. Rev. Lett.* **100** 225001
[24] Goncharov V N *et al* 2010 *Phys. Rev. Lett.* **104** 165001
[25] Amendt P A *et al* 2009 *Plasma Phys. Control. Fusion* **51** 124048
[26] Amendt P A *et al* 2010 *Phys. Rev. Lett.* **105** 115005
[27] Li C K *et al* 2006 *Phys. Rev. Lett.* **97** 135003
[28] Petrasso R D *et al* 2009 *Phys. Rev. Lett.* **103** 085001
[29] Frenje J A *et al* 2009 *Phys. Plasmas* **16** 022702
[30] Séguin F H *et al* 2002 *Phys. Plasmas* **9** 2725
[31] Petrasso R D *et al* 1996 *Phys. Rev. Lett.* **77** 2718
[32] Mackinnon A J *et al* 2006 *Phys. Rev. Lett.* **97** 045001
[33] Philippe F *et al* 2010 *Phys. Rev. Lett.* **104** 035004
[34] Robey H F *et al* 2010 *Phys. Plasmas* **17** 056313
[35] MacFarlane J J 2003 *J. Quant. Spectrosc. Radiat. Transfer* **81** 287
[36] Li C K *et al* 2007 *Phys. Rev. Lett.* **99** 015001
[37] Li C K *et al* 2009 *Phys. Rev.* E **80** 016407
[38] Jackson J D 1975 *Classical Electrodynamics* (New York: Wiley)
[39] Lasinski T A *et al* 1973 *Rev. Mod. Phys.* **45** s1
[40] Glenzer S H *et al* 1999 *Phys. Plasmas* **6** 2117
[41] Haan S W *et al* 2004 *Nucl. Fusion* **44** S171
[42] Haan S W *et al* 2005 *Phys. Plasmas* **12** 056316
[43] Hey D S *et al* 2008 *Rev. Sci. Instrum.* **79** 053501